The Bioscan AN INTERNATIONAL QUARTERLY JOURNAL OF LIFE SCIENCES 21(2):S.I(2), 148-176, 2026 www.thebioscan.com

Temperature-Driven Phase Evolution and Physicochemical Property changes in TiO_2 Nanoparticles

Anantha Prabhu C [a,e], Silambarasan D [*, b,e], Uma Maheshwari J [c,e], Subramonian K [d,e]

[a] *Research Scholar (Reg.No: 21211072131001), PG and Research Department of Physics, The M.D.T. Hindu College, Tirunelveli - 627 010, Tamil Nadu, India.*
[b] *Assistant Professor, PG and Research Department of Physics, The M.D.T. Hindu College, Tirunelveli - 627 010, Tamil Nadu, India.*
[c] *Associate Professor, PG and Research Department of Physics, The M.D.T. Hindu College, Tirunelveli - 627 010, Tamil Nadu, India.*
[d] *Associate Professor, Department of Botany, The M.D.T. Hindu College, Tirunelveli - 627 010, Tamil Nadu, India.*
[e] *Affiliated to Manonmaniam Sundaranar University, Abishekapatti, Tirunelveli - 627 012, Tamil Nadu, India.*
[*]*Corresponding author Email: carbonlabmdt@gmail.com, silambarasan@mdthinducollege.org*

DOI: https://doi.org/10.63001/tbs.2026.v21.i02.S.I(2).pp148-176

KEYWORDS

TiO_2 nanoparticles; sol–gel synthesis; annealing temperature; anatase-to-rutile phase transformation; cyclic voltammetry

Received on:
16-02-2026

Accepted on:
14-03-2026

Published on:
11-04-2026

Abstract

TiO_2 nanoparticles were synthesized by the sol–gel method and annealed at 450, 550, 650, and 750 °C. This allowed examination of how temperature drives phase evolution and alters structural, optical, vibrational, thermal, and electrochemical properties. X-ray diffraction (XRD) analysis confirmed phase-pure anatase at 450 and 550 °C. At 650 °C a mixed anatase and rutile structure appeared. At 750 °C there was complete conversion to the rutile phase is noted. Crystallite size grew monotonically from 21.3 nm to 40.9 nm, while dislocation density and microstrain fell sharply across the same range, indicating progressive defect annihilation. UV–Vis spectroscopy (UV-Vis) revealed a systematic red-shift in the optical absorption edge from ~390 to ~416 nm. Fourier Transform Infrared Spectroscopy (FTIR) showed progressive loss of surface hydroxyl groups and organic residues, with the Ti–O lattice sharpening and intensifying at higher temperatures. Photoluminescence (PL) measurements indicated a shift in emission followed by intensity quenching at 750 °C due to reduced defect density. Raman spectra corroborated the XRD-determined phase sequence and further confirmed the anatase to rutile phase transformation. Thermogravimetric analysis (TGA) showed total weight loss falling from ~6% (450 °C) to ~0.5% (750 °C), confirming the removal of adsorbed water and organic precursors with increasing crystallinity. Cyclic voltammetry (CV) indicated that the 450 °C sample delivered the highest specific capacitance value of 1.311 F g^{-1} at 10 mV s^{-1} due to its greater surface area and defect-rich anatase structure. Electrochemical impedance spectroscopy confirmed the lowest charge-transfer resistance in the 450 °C sample. The 450 °C anatase sample additionally exhibited measurable antibacterial activity against *S. aureus*, *B. subtilis*, and *K. pneumoniae.* Together, these results establish a consistent, temperature-indexed property map that can guide the selection of TiO_2 annealing conditions for photocatalysis, energy storage, and optoelectronic applications.

1.Introduction

Titanium dioxide (TiO_2) is one of the most extensively studied metal oxide semiconductors, owing to a combination of chemical stability, non-toxicity, and a band gap that can be manipulated through phase control and microstructural tuning. Among its three anatase, rutile, and brookite crystalline polymorphs, anatase and rutile have attracted the greatest research interest. Anatase, metastable at macroscopic scales, carries a direct band gap of ~3.2 eV and shows high photocatalytic activity largely due to its favourable conduction-band position and the greater electron mobility compared with rutile[1,2]. Rutile, the thermodynamically stable polymorph above ~600 °C, has a narrower band gap of ~3.0 eV and a higher refractive index, properties that make it preferred for pigment, dielectric, and certain optoelectronic uses [3]. In practice, both phases coexist across a range of applications, and understanding precisely how synthesis conditions shift the phase balance is central to materials engineering.

Considerable work has addressed individual aspects of this temperature effect on TiO_2 nanoparticles. Hanaor and Sorrell [3] provided an authoritative review of the anatase-to-rutile transformation, cataloguing the roles of grain size, surface area, and impurities in setting the transition temperature. Zhang and Banfield [4,5] introduced the thermodynamic and kinetic framework showing that below a critical crystallite size of ~14 nm anatase is more stable than rutile because of the lower surface enthalpy of the {101} facet; above this size rutile becomes favourable and nucleates at anatase grain boundaries. Luttrell et al. [2] used epitaxial model films to clarify that the superior photocatalytic performance of anatase over rutile arises from differences in carrier mobility and recombination rate rather than simply from band gap width. On the optical side, Muthee and Dejene [6] reported anatase at 450 °C, anatase/rutile mixtures at 550–650 °C, and rutile at 750 °C for sol-gel TiO_2 nanoparticles, with larger crystal and grain sizes and lower surface area at higher temperatures. Alaya et al. [7] and Sharma and Kumar [8] extended these optical observations to spray-pyrolysis and thin-film geometries, respectively. FTIR and thermal studies by Nolan et al. [9] and Vasconcelos et al. [10] traced the loss of surface hydroxyl groups and the evolution of Ti–O lattice modes as functions of calcination temperature, while Henderson [11] and Busca [12] provided the mechanistic context for surface dehydroxylation.

On the photoluminescence side, Plugaru et al. [13] examined oxygen-vacancy and Ti^{3+} defect levels in TiO_2. For electrochemical performance, Prasannalakshmi et al. [14] demonstrated that the anatase polymorph supports higher specific capacitance than rutile in supercapacitor configurations, attributing the difference to the greater active surface area and lower charge-transfer resistance of the less-ordered phase. These individual studies collectively establish qualitative trends, but rarely combine all measurement modalities on the same sample series, making cross-property comparisons difficult. A concise, cross-technique dataset that includes all of these responses for a single sample series is essential both for fundamental understanding and for making informed processing decisions.

Beyond energy and optical applications, TiO_2 nanoparticles have attracted increasing attention for their antibacterial activity due to their chemical stability and ability to generate reactive oxygen species that disrupt bacterial cell membranes through surface hydroxyl chemistry even in the absence of UV activation [15,16]. Smaller crystallite sizes, typically below ~ 25 nm, have been reported to amplify this contact-mediated effect by increasing the proportion of chemically active surface sites [15,16]. Given that the 450 °C sample in this study combines the smallest crystallite size with the highest surface hydroxyl density and lowest charge-transfer resistance, its antibacterial performance against clinically relevant Gram-positive and Gram-negative strains was also evaluated to extend the property map beyond electrochemical and optical characterisation.

A gap, therefore, remains. A self-consistent, single-batch study that follows the same four-temperature series through XRD, UV–Vis, FTIR, Raman, photoluminescence, TGA, cyclic voltammetry and antibacterial activity simultaneously is a much needed one. The present work addresses this gap by synthesising TiO_2 nanoparticles via a sol–gel route and annealing at 450, 550, 650, and 750 °C under identical conditions. The resulting samples are characterised by all techniques listed above. The goal is to provide an internally consistent property map that traces the structural, optical, vibrational, thermal, and electrochemical properties and antibacterial potential of the material that responds to the same progression of annealing temperature and the accompanying phase transformation. This dataset can serve as a basis for selecting optimal TiO_2 annealing conditions tailored to photocatalysis,

energy storage, and optoelectronic applications.

2. Materials and Methods

2.1. Materials

Titanium (IV) isopropoxide (97%, Sigma-Aldrich) and isopropyl alcohol (≥99%, Merck) were employed as precursor, and deionized water as solvent were used for the synthesis of TiO_2 nanoparticles. All glassware used in the experiment was procured from Borosil.

2.2. Synthesis of TiO_2 nanoparticles

Titanium (IV) isopropoxide (TTIP) was ultrasonicated for 30 minutes to minimize vapor formation and ensure uniform precursor stabilization. Next, 90 mL of isopropyl alcohol was gradually added with TTIP under stirring. The texture of the solution immediately changed from colourless to pale yellow, indicating precursor interaction. The mixture was then stirred for 20 minutes to achieve homogeneity. Hydrolysis was initiated by drop wise addition of 10 mL deionized water under vigorous stirring, the solution to transition from pale yellow to milky white and confirming TiO_2 sol formation. The mixture was continuously stirred for 4 hours to complete hydrolysis and condensation reactions. The sol aged overnight to form a gel. The obtained gel was subsequently centrifuged and washed multiple times with deionized water and ethanol to remove impurities and unreacted precursors. The purified product was dried in a hot air oven at 100 °C for 2.5 hours to remove moisture and volatiles, then calcined at 450 °C for 4 hours to obtain crystalline TiO_2 nanoparticles [17]. Additional samples were prepared under identical conditions at annealing temperatures of 550, 650, and 750 °C to study temperature-dependent phase and structural, physicochemical property evolution.

3. Result and Discussion

3.1. Structural Properties (XRD)

Figure 1 presents the stacked XRD patterns of TiO_2 nanoparticles annealed at 450, 550, 650, and 750 °C. The sample annealed at 450 °C exhibits characteristic diffraction peaks at $2\theta \approx 25.29°$, 37.68°, 47.96°, 54.02°, 54.63°, 62.70°, 69.43°, 70.38°, and 75.04°. These correspond to the (101), (004), (200), (105), (211), (204), (116), (220), and (215) planes of the tetragonal anatase structure [18]. These positions are in excellent agreement with the reference card JCPDS 21-1272, confirming phase-pure anatase formation. Scherrer analysis yields crystallite sizes spanning from 7.0 to 51.7 nm, with an average of 21.3 nm. This wide distribution

reflects non-uniform nucleation and growth kinetics at a lower annealing temperature of 450 °C. The dislocation density and microstrain were calculated along with particle size determination and presented in Table 1. The mean dislocation density $\delta = 7.11 \times 10^{-3}$ nm^{-2} and mean microstrain $\varepsilon = 6.65 \times 10^{-3}$ are the highest values observed. This suggests significant lattice distortion and defect concentration at this stage. Such levels are typical for low-temperature annealed nanostructured TiO_2 [1–3].

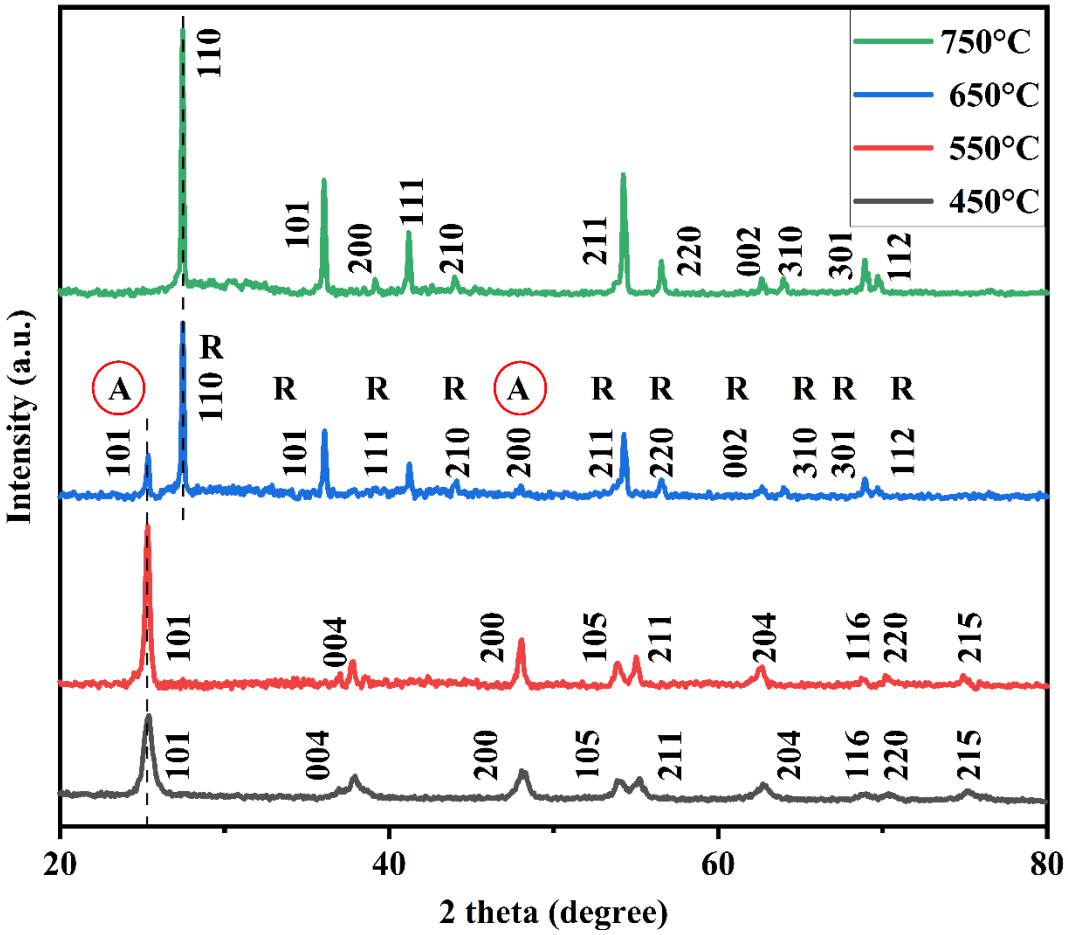

Figure 1. Stacked XRD patterns of TiO_2 nanoparticles annealed at 450, 550, 650, and 750 °C

Upon annealing at 550 °C, the diffraction peaks become sharper and more intense, while the anatase phase is maintained. This indicates enhanced crystallinity without phase transformation. The reduction in full width at half maximum (FWHM) reflects an increase in crystallite size (~25.1 nm). This change is attributed to thermally driven grain growth. All nine reflections observed at 450 °C are retained at essentially identical 2θ positions (25.31°, 37.77°, 48.01°, 53.93°, 55.03°, 62.56°, 68.81°, 70.28°, and 74.93°). Negligible peak shifts of ≤ 0.05° confirm

the absence of compositional or significant strain-induced lattice distortion. Importantly, no rutile-phase reflections are discernible. This confirms that the anatase-to-rutile phase boundary has not been crossed at this temperature under the present synthesis conditions.

Table 1. Structural parameters of TiO_2 nanoparticles annealed at 450 °C (anatase phase, JCPDS 21-1272).

2θ (°)	θ (°)	hkl	d-spacing (Å)	FWHM β (°)	D (nm)	δ ×10⁻³ (nm⁻²)	ε ×10⁻³
25.290	12.645	101	3.519	0.678	12.004	6.940	13.191
37.679	18.840	004	2.385	1.194	7.032	20.225	15.266
47.958	23.979	200	1.895	0.844	10.303	9.420	8.278
54.017	27.008	105	1.696	0.419	21.258	2.213	3.591
54.631	27.315	211	1.679	1.212	7.380	18.361	10.236
62.703	31.351	204	1.481	0.605	15.381	4.227	4.332
69.425	34.713	116	1.353	0.226	42.778	0.546	1.423
70.385	35.192	220	1.337	0.188	51.683	0.374	1.164
75.043	37.522	215	1.265	0.414	24.169	1.712	2.355
				Average	**21.33**	**7.113**	**6.648**

(Bragg angle (θ), interplanar spacing (d), FWHM (β), crystallite size (D) from the Scherrer equation, dislocation density (δ), microstrain (ε), and Miller indices (hkl))

The retention of pure anatase at 550 °C can be understood through the size-dependent thermodynamic framework proposed by Zhang and Banfield [5] Below a critical crystallite size of ~14 nm, anatase is thermodynamically more stable than rutile due to the lower surface enthalpy of the {101} anatase facet. The mean dislocation density drops sharply from 7.11 × 10^{-3} to 1.88 × 10^{-3} nm^{-2}, and the mean microstrain decreases from 6.65 × 10^{-3} to 3.48 × 10^{-3}. These reductions are physically explained by thermal annihilation [1,3,4].

The XRD pattern of the 650 °C sample marks the onset of the irreversible anatase-to-rutile phase transformation. The anatase (101) reflection at 25.34° and the (200) reflection at 48.01° are still discernible, indicating residual anatase. Strong new reflections appear at 27.46°, 36.08°, 41.24°, 44.04°, 54.29°, 56.56°, 62.66°, 64.01°, 68.92°, and 69.68°. This

indicates the tetragonal rutile polymorph, indexed to planes (110), (101), (111), (210), (211), (220), (002), (310), (301), and (112), consistent with JCPDS card no. 01-076-1939. At 650 °C, the average crystallite size is 37.6 nm, a 49.8% increase over the 550 °C value (25.1 nm). This is markedly larger than the 17.8% increase observed between 450 and 550 °C. The accelerated grain growth across the transformation boundary is attributable to higher atomic mobility at 650 °C and the exothermic nature of the anatase to rutile transformation. Mean dislocation density and microstrain continue their monotonic decline to 0.798 × 10^{-3} nm^{-2} and 2.46 × 10^{-3}, respectively, demonstrating progressive structural ordering [1,3,4].

Table 2. Structural parameters of TiO_2 nanoparticles annealed at 550 °C (anatase phase, JCPDS 21-1272).

2θ (°)	θ (°)	hkl	d-spacing (Å)	FWHM β (°)	D (nm)	δ ×10^{-3} (nm^{-2})	ε ×10^{-3}
25.313	12.657	101	3.516	0.336	24.240	1.702	6.526
37.773	18.887	004	2.380	0.295	28.498	1.231	3.758
48.010	24.005	200	1.893	0.352	24.727	1.636	3.446
53.932	26.966	105	1.699	0.537	16.608	3.625	4.603
55.025	27.512	211	1.668	0.313	28.634	1.220	2.621
62.564	31.282	204	1.483	0.573	16.219	3.801	4.116
68.806	34.403	116	1.363	0.370	26.053	1.473	2.355
70.279	35.140	220	1.338	0.367	26.504	1.424	2.272
74.928	37.464	215	1.266	0.290	34.531	0.839	1.650
				Average	**25.11**	**1.883**	**3.483**

Further annealing at 750° C results in a predominantly rutile phase. This is evidenced by the disappearance of anatase reflections and the dominance of rutile peaks. The anatase (101) reflection at ~25.3° is vanished. A new weak peak at 31.9° appears, corresponding to an additional rutile reflection. Eleven indexed peaks at 27.44°, 36.05°, 39.17°, 41.21°, 44.02°, 54.27°, 56.56°, 62.66°, 63.99°,

68.94°, and 69.73° are exclusively attributable to the rutile polymorph with planes (110), (101), (200), (111), (210), (211), (220), (002), (310), (301), and (112), respectively. The peaks become sharper with increased intensity, indicating improved crystallinity and grain coarsening. The average crystallite size at 750 °C is 40.9 nm, which represents only an 8.6% increase over the value of 37.6 nm obtained at 650 °C. This suggests a deceleration in grain growth rate as the system approaches the thermodynamic equilibrium grain size for this temperature. The dislocation density and microstrain decrease to 0.641 × 10^{-3} nm^{-2} and 2.117 × 10^{-3}, respectively, reflecting a highly crystalline, defect-minimised rutile lattice with superior structural order [3,4].

Table 3. Structural parameters of TiO_2 nanoparticles annealed at 650 °C (anatase phase - JCPDS 21-1272, rutile phase – JCPDS 01-076-1939)

2θ (°)	θ (°)	hkl	d-spacing (Å)	FWHM β (°)	D (nm)	δ ×10^{-3} (nm^{-2})	ε ×10^{-3}
25.337	12.668	101 (A)	3.512	0.190	42.788	0.546	3.694
27.460	13.730	110 (R)	3.245	0.176	46.400	0.464	3.148
36.082	18.041	101 (R)	2.487	0.202	41.337	0.585	2.708
41.237	20.618	111 (R)	2.187	0.238	35.602	0.789	2.765
44.039	22.019	210 (R)	2.055	0.324	26.485	1.426	3.491
48.006	24.003	200 (A)	1.894	0.190	45.703	0.479	1.865
54.290	27.145	211 (R)	1.688	0.293	30.456	1.078	2.495
56.561	28.280	220 (R)	1.626	0.287	31.406	1.014	2.330
62.662	31.331	002 (R)	1.481	0.341	27.307	1.341	2.441
64.012	32.006	310 (R)	1.453	0.217	43.071	0.539	1.518
68.923	34.462	301 (R)	1.361	0.208	46.372	0.465	1.321
69.676	34.838	112 (R)	1.348	0.281	34.427	0.844	1.763
				Average	**37.61**	**0.798**	**2.461**

(A =Anatase peak; R = Rutile peak)

Table 4. Structural parameters of TiO_2 nanoparticles annealed at 750 °C (rutile phase, JCPDS 01-076-1939).

2θ (°)	θ (°)	hkl	d-spacing (Å)	FWHM β (°)	D (nm)	δ ×10⁻³ (nm⁻²)	ε ×10⁻³
27.443	13.722	110	3.247	0.162	50.595	0.391	2.888
36.053	18.026	101	2.489	0.191	43.848	0.520	2.555
39.174	19.587	200	2.298	0.165	51.105	0.383	2.023
41.208	20.604	111	2.189	0.202	41.931	0.569	2.349
44.020	22.010	210	2.055	0.265	32.286	0.959	2.865
54.272	27.136	211	1.689	0.244	36.562	0.748	2.079
56.558	28.279	220	1.626	0.217	41.581	0.578	1.760
62.661	31.330	002	1.481	0.203	45.876	0.475	1.453
63.991	31.996	310	1.454	0.254	36.918	0.734	1.772
68.938	34.469	301	1.361	0.287	33.583	0.887	1.824
69.731	34.865	112	1.347	0.275	35.246	0.805	1.720
				Average	**40.87**	**0.641**	**2.117**

The monotonic reduction in dislocation density (from 7.11 to 0.641 × 10^{-3} nm^{-2}) and microstrain (from 6.65 to 2.117 × 10^{-3}) across the series demonstrates that thermal annealing progressively drives the material toward a thermodynamically optimal crystalline state. The XRD results confirm that increasing annealing temperature induces crystallite growth, reduction in lattice defects and microstrain, and phase transformation from anatase to rutile. Systematic peak sharpening, intensity enhancement, and reduction in FWHM are direct consequences of thermally activated grain growth and defect relaxation. Minor peak shifts observed across the samples are attributed to lattice strain relaxation and corresponding changes in interplanar spacing during annealing. Disappearance of anatase

reflections and sharpening of rutile peaks at 750 °C in Table 4 confirms the phase transformation completion. Table 5 presents a consolidated summary of the average structural parameters extracted from the four annealing conditions. This format facilitates direct inter-sample comparison. The monotonic trends in all parameters across the 450–750 °C series are physically self-consistent and provide strong internal validation of the measurement quality.

Table 5. Consolidated structural parameters of TiO_2 nanoparticles as a function of annealing temperature.

Sample	Avg. D (nm)	D range (nm)	Avg. δ ×10⁻³ (nm⁻²)	Avg. ε ×10⁻³	Phase	JCPDS
TiO_2 – 450 °C	21.3	7.0–51.7	7.11	6.65	Anatase	21-1272
TiO_2 – 550 °C	25.1	16.2–34.5	1.88	3.48	Anatase	21-1272
TiO_2 – 650 °C	37.6	26.5–46.4	0.798	2.46	Anatase Rutile	21-1272 01-076-1939
TiO_2 – 750 °C	40.9	32.3–51.1	0.641	2.12	Rutile	01-076-1939

3.2. Vibrational Properties (Raman)

To investigate phase evolution, lattice dynamics, and crystallinity changes, Raman spectroscopy was employed for TiO_2 nanoparticles annealed at 450, 550, 650, and 750 °C, The Raman modes shown in Figure 2 demonstrate a strong dependence on annealing temperature, indicating progressive structural and phase transition behaviour.

At 450 °C, the Raman spectrum exhibits characteristic anatase vibrational modes located at 143, 398, 515, and 639 cm^{-1}, corresponding to the E_g, B_{1g}, A_{1g}, and E_g modes of anatase TiO_2, respectively [19]. However, these peaks display relatively low intensity and broad linewidth, indicating poor crystallinity, small crystallite size, and higher lattice disorder at this annealing temperature. The dominance of the E_g mode at ~143 cm^{-1} confirms the presence of anatase as the primary phase [20].

Upon increasing the annealing temperature to 550 °C, the Raman modes

slightly shift to lower wavelengths at 130, 386, 508, and 636 cm^{-1}, accompanied by a significant increase in peak intensity and narrowing. The observed red-shift of the E_g mode (from ~143 to ~130 cm^{-1}) is indicative of phonon confinement relaxation and crystallite growth, while the enhanced intensity suggests improved long-range ordering. This behaviour is consistent with the reduction of structural defects and grain boundary density during thermal annealing [4,20].

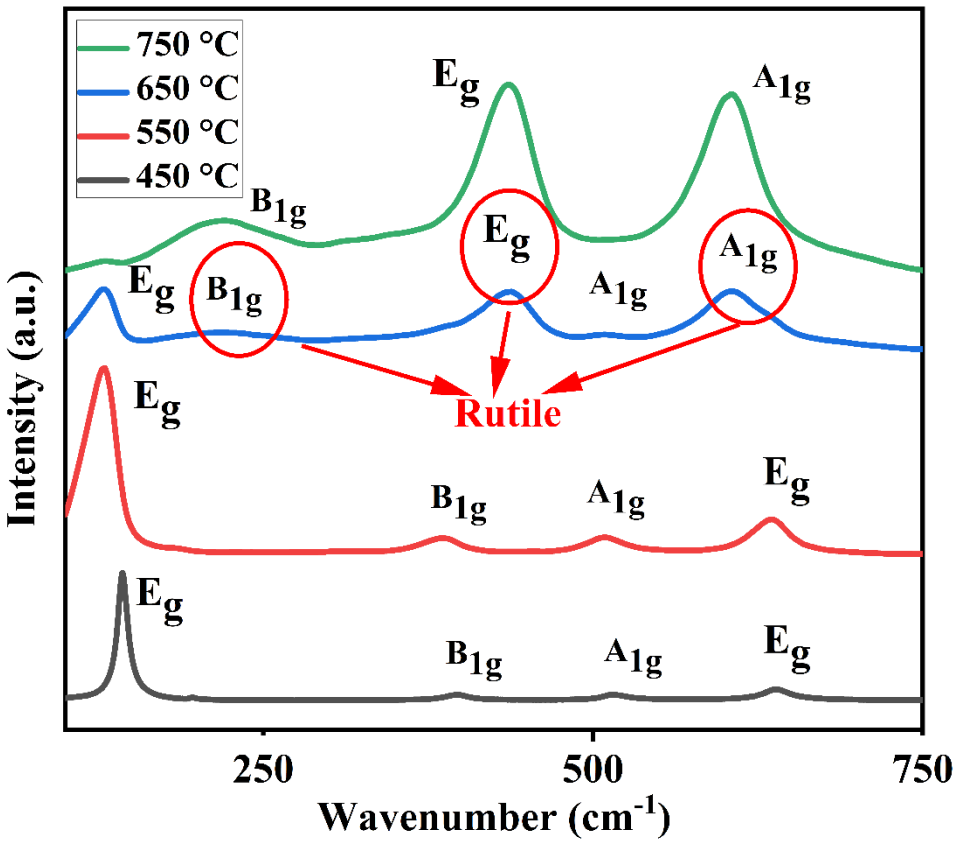

Figure 2. Raman spectra of TiO_2 nanoparticles annealed at 450, 550, 650, and 750 °C

At 650 °C, the Raman spectrum undergoes a substantial transformation, where new vibrational modes emerge at 130, 216, 438, 510, and 606 cm^{-1}, alongside the persistence of modified anatase features. The appearance of peaks at ~216, ~438, and ~606 cm^{-1} corresponds to the B_{1g}, E_g, and A_{1g} modes of the rutile phase, indicating the onset of the anatase-to-rutile phase transition. The coexistence of both anatase (~130, 510 cm^{-1}) and rutile (~216, 438, 606 cm^{-1}) signatures confirms a

mixed-phase system, which is thermodynamically expected in this temperature regime [4,21].

At the highest annealing temperature of 750 °C, Raman spectrum shows the complete disappearance of anatase modes, while only rutile-related peaks remain at 222, 436, and 606 cm^{-1} with significantly enhanced intensity and sharpness. This clearly indicates a full phase transformation to rutile TiO_2, accompanied by increased crystallite size and reduced lattice defects. The high intensity and narrow linewidth of these peaks reflect improved crystallinity and long-range order. The absence of anatase E_g mode further confirms the complete structural transition [21].

The observed Raman evolution correlates with the thermodynamically driven anatase to rutile conversion at elevated temperatures (~600–700 °C). Shifts, disappearance, and emergence of Raman modes are governed by phonon confinement effects, lattice distortion, oxygen vacancy redistribution, and grain growth kinetics [20]. Red-shift and intensity increase at intermediate temperatures arise from reduced phonon scattering and increased crystallite size, while rutile mode dominance at higher temperatures reflects phase stability.

Furthermore, the Raman results are in strong agreement with the XRD analysis, where the progressive disappearance of anatase diffraction peaks and emergence of rutile reflections confirm the same phase evolution trend. The combined structural and vibrational analysis provides robust evidence for temperature-induced crystallographic transformation and defect minimization in TiO_2 nanoparticles.

3.3. Optical Properties (UV–Vis Spectroscopy)

The UV absorbance spectra of TiO_2 nanoparticles annealed at 450, 550, 650, and 750 °C shown in Figure 3, exhibit a strong UV absorption edge that systematically red-shifts with increasing annealing temperature.

The absorption onset moves to longer wavelengths with higher annealing temperature. This indicates band gap narrowing. The narrowing is attributed to both crystallite growth and phase change. The comparatively higher apparent band gap at this temperature (450 °C) is mainly attributed to defect states and surface disorder, rather than quantum confinement effects. As grains grow (550–750 °C), quantum confinement weakens and rutile [22] forms, producing a lower gap [7,8].

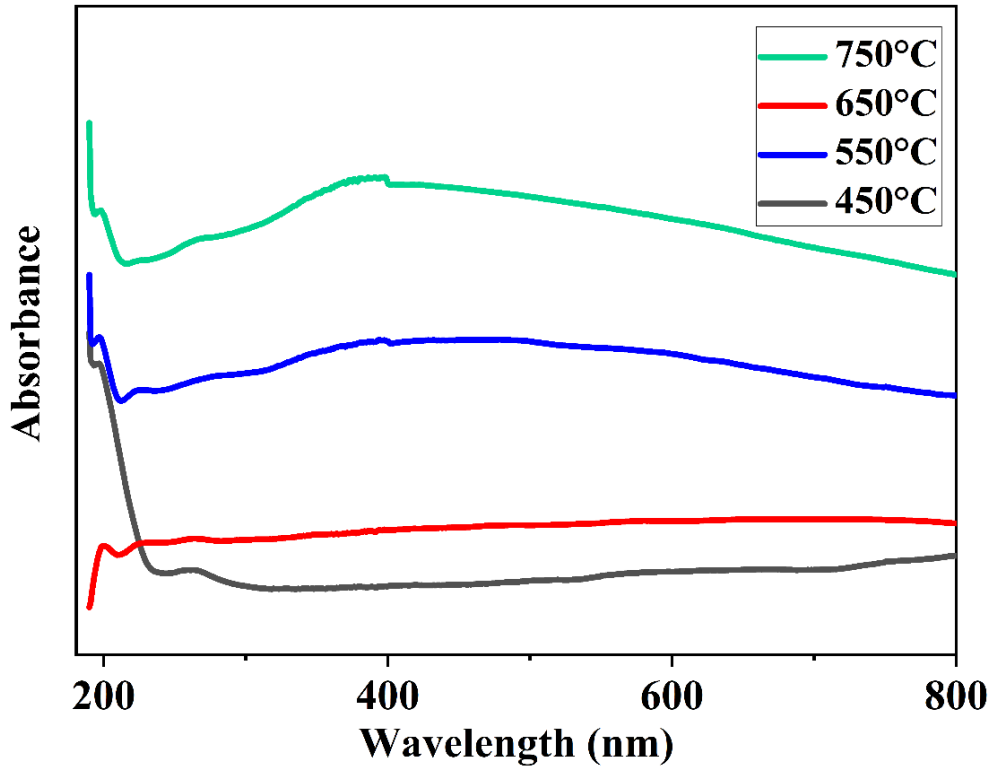

Figure 3. UV absorbance spectra of TiO_2 nanoparticles annealed at 450, 550, 650, and 750 °C

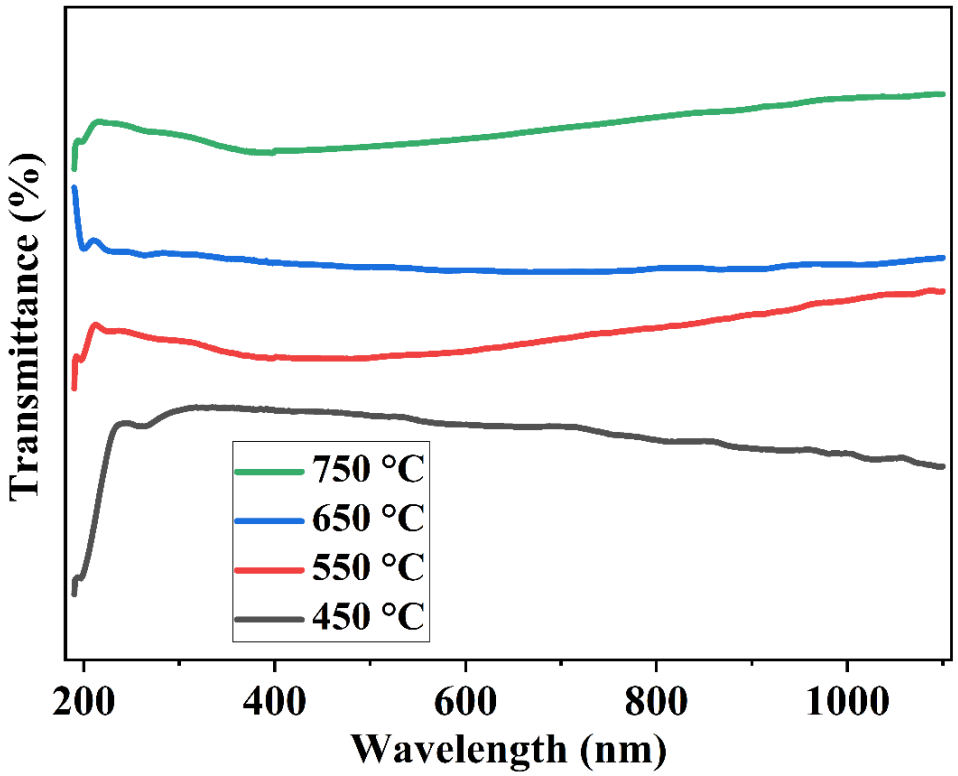

Figure 4. UV transmittance spectra of TiO_2 nanoparticles annealed at 450, 550, 650, and 750 °C

The UV transmittance spectra of TiO_2 nanoparticles annealed at 450, 550, 650, and 750 °C in Figure 4 show high transparency beyond ~400 nm and a sharp absorption edge in the UV region. The absorption edge shifts from ~390 nm at 450 °C to ~416 nm at 750 °C. This indicates a reduction in the optical band gap. The Urbach tail shortens upon annealing, reflecting reduced disorder and defect states. Enhanced crystallinity and phase evolution cause systematic changes in the optical properties [7,8,22].

The optical changes align with the XRD results, that larger crystallites and decreased strain correlate with narrower band gaps. The onset of rutile at 650–750 °C causes a perceptible change in the spectral slope. High transmittance (>98%) beyond 500 nm at all temperatures confirms that samples remain free of visible absorbers. This implies phase purity. The emergence of rutile peaks at 650–750 °C in XRD coincides with the largest optical red-shift.

3.4. Vibrational Properties (FTIR)

The FTIR spectra of TiO_2 nanoparticles annealed at 450, 550, 650, and 750 °C in Figure 5 reveal significant structural and chemical evolution as a function of thermal treatment.

At lower calcination temperatures (450 and 550 °C), the spectra exhibit a prominent broad absorption band in the range of 3400–3430 cm^{-1}, which is attributed to O–H stretching vibrations of physically adsorbed water molecules and surface hydroxyl groups. Additionally, a distinct H–O–H bending vibration is observed at ~1630 cm^{-1}, confirming the presence of physisorbed water within the TiO_2 matrix [10,23]. The spectra also display weak C–H stretching bands at ~2929 and 2850 cm^{-1}, indicating residual organic species from synthesis, along with characteristic Ti–O lattice vibrations appearing in the lower wavenumber region (~500 cm^{-1}) [24,25].

With an increase in annealing temperature to 650 °C, the intensity of the O–H stretching and H–O–H bending bands decreases significantly, indicating progressive dehydration and dehydroxylation of the surface [9,10]. Simultaneously, the Ti–O lattice vibration near ~500 cm^{-1} becomes more pronounced, reflecting improved crystallinity and enhanced structural ordering within the TiO_2 framework [24].

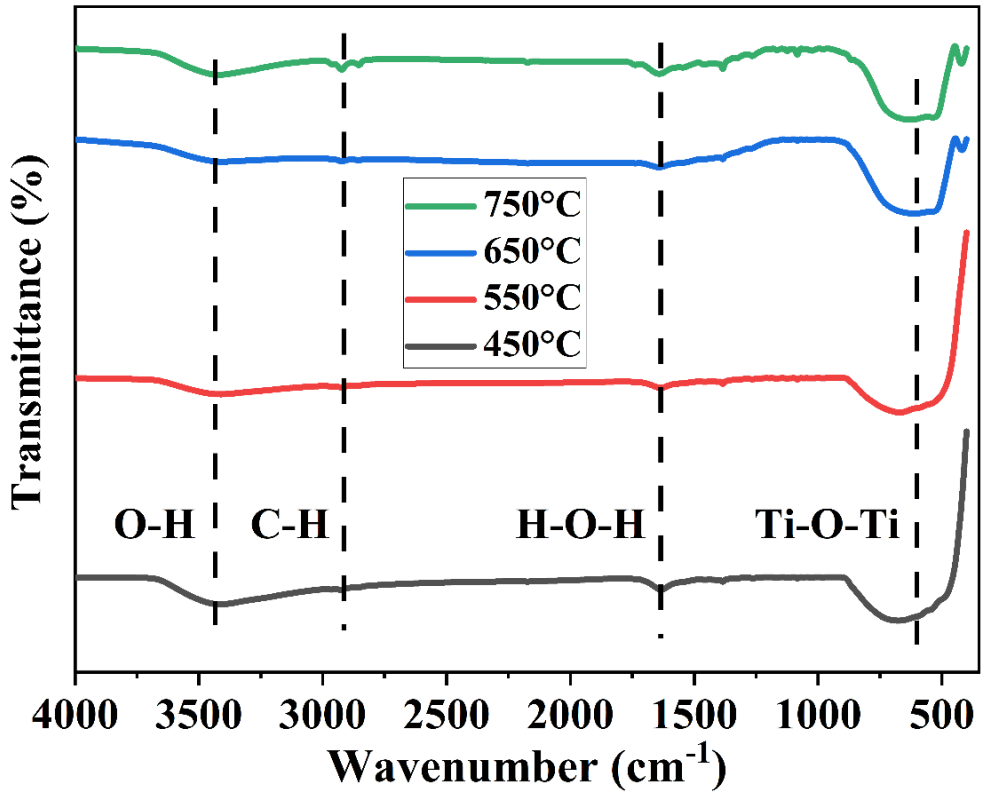

Figure 5. FTIR spectra of TiO_2 nanoparticles annealed at 450, 550, 650, and 750 °C

750 °C, the broad O–H band (~3400 cm^{-1}) and the C–H stretching peaks (~2929 and 2850 cm^{-1}) disappear completely, confirming the removal of surface hydroxyl groups and organic residues [24,25]. In contrast, a sharp and intense Ti–O vibrational band emerges in the range of 500–600 cm^{-1}, which is associated with increased crystallinity and the transformation from anatase to the thermodynamically stable rutile phase [9,17]. The significant sharpening of this band further indicates lattice densification and improved long-range order.

Overall, the FTIR spectra demonstrate a clear transition from hydroxyl-rich, partially disordered structures at lower temperatures to highly crystalline TiO_2 at elevated temperatures. The progressive disappearance of O–H and organic bands, along with the dominance of Ti–O lattice vibrations, confirms that annealing effectively removes surface-bound species and enhances phase stability. These observations are in strong agreement with previously reported FTIR studies of thermally treated TiO_2 nanostructures [9,10,23]. Notably, the residual band near ~1630 cm^{-1} persists up to 650 °C and becomes very weak at 750 °C, indicating gradual removal of chemically bound hydroxyl species [10]. Thus, annealing primarily facilitates dehydration, organic decomposition, and phase transformation,

resulting in structurally stable and phase-pure TiO_2.

3.5. Photoluminescence Properties (PL)

PL spectra of TiO_2 nanoparticles annealed at 450, 550, 650, and 750 °C in Figure 6 show a strong temperature-dependent shift and intensity variation. At 450 °C a broad red emission appears around ~610 nm, which we attribute to self-trapped excitons or defect-related states. As the temperature rises to 550°C the PL peak red-shifts into the near-infrared ~ 784 nm and its intensity increases. Again, when the temperature rises to 650 °C the excitation peak is shifted to ~ 804 nm and the intensity increases. This large NIR emission is attributed to oxygen-vacancy and Ti^{3+} defect states, which introduce mid-gap energy levels that facilitate radiative recombination in TiO_2 and correlates with formation of rutile [13,26,27]. The emergence of rutile phase begins to influence the emission behaviour. Notably, rutile TiO_2 is known to exhibit a sharp emission near 800 nm, further supporting the phase transition contribution.

At 750 °C, the NIR peak ~804 nm remains prominent but show slightly weaker intensity, this reduction is attributed to increased crystallinity and grain growth, which reduce defect density and enhance non-radiative recombination pathways. The dominance of the rutile phase at this temperature leads to a more ordered lattice structure with fewer active luminescent defect centres [13,26,27].

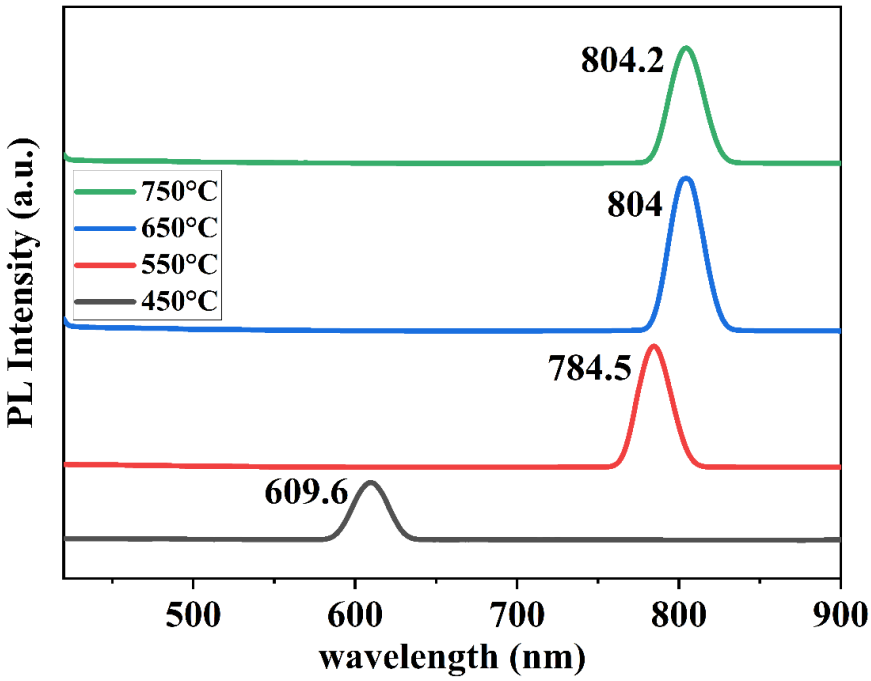

Figure 5. Photoluminescence spectra of TiO_2 nanoparticles annealed at 450, 550, 650, and 750 °C

Overall, the PL behaviour demonstrates that annealing initially enhances emission through the generation of oxygen vacancies and Ti^{3+} defect states, followed by quenching at higher temperatures due to improved crystallinity and reduced defect concentration. The observed red-shift from the visible (~610 nm) to near-infrared (~804 nm) region clearly indicates the transition from anatase-related emission to rutile-associated defect emission. These findings are consistent with reported literature on defect-mediated photoluminescence and phase transformation in TiO_2 systems. This behaviour mirrors the phase evolution observed in XRD and Raman analyses.

3.6 Thermal Properties (TGA)

Thermogravimetric analysis (TGA) was performed to evaluate the thermal stability, decomposition behaviour, and surface chemistry evolution of TiO_2 nanoparticles annealed at 450, 550, 650, and 750 °C, as presented in Figure 5. The weight loss profiles exhibit distinct temperature-dependent features, reflecting progressive removal of adsorbed species, residual organics, and structural stabilization with increasing annealing temperature.

At 450 °C, the TGA curve shows a gradual and continuous weight loss (~6%) over the entire temperature range. An initial weight reduction below ~100 °C (around 83 °C) is attributed to the removal of physically adsorbed water molecules. The subsequent weight loss observed near ~330 °C corresponds to the decomposition of residual organic precursors and surface hydroxyl groups. Beyond ~630 °C, a slight increase or minor fluctuation in the curve is observed, which may arise likely associated with instrumental artefacts or baseline instability. The relatively higher total weight loss indicates that the sample retains significant surface-bound species and incomplete crystallization at this annealing temperature [11,12].

At 550 °C, the TGA profile exhibits a more defined multi-step decomposition behaviour, with noticeable weight loss stages around 93, 227, 417, and 570 °C, resulting in an overall weight loss of approximately ~5%. The initial loss below 100 °C is again associated with adsorbed moisture removal, while the intermediate stages (~200–450 °C) correspond to dehydroxylation and decomposition of residual organics. The reduced total weight loss compared to the 450 °C sample indicates improved thermal stability and reduced surface contamination, suggesting enhanced crystallinity due to higher annealing temperature [4,12].

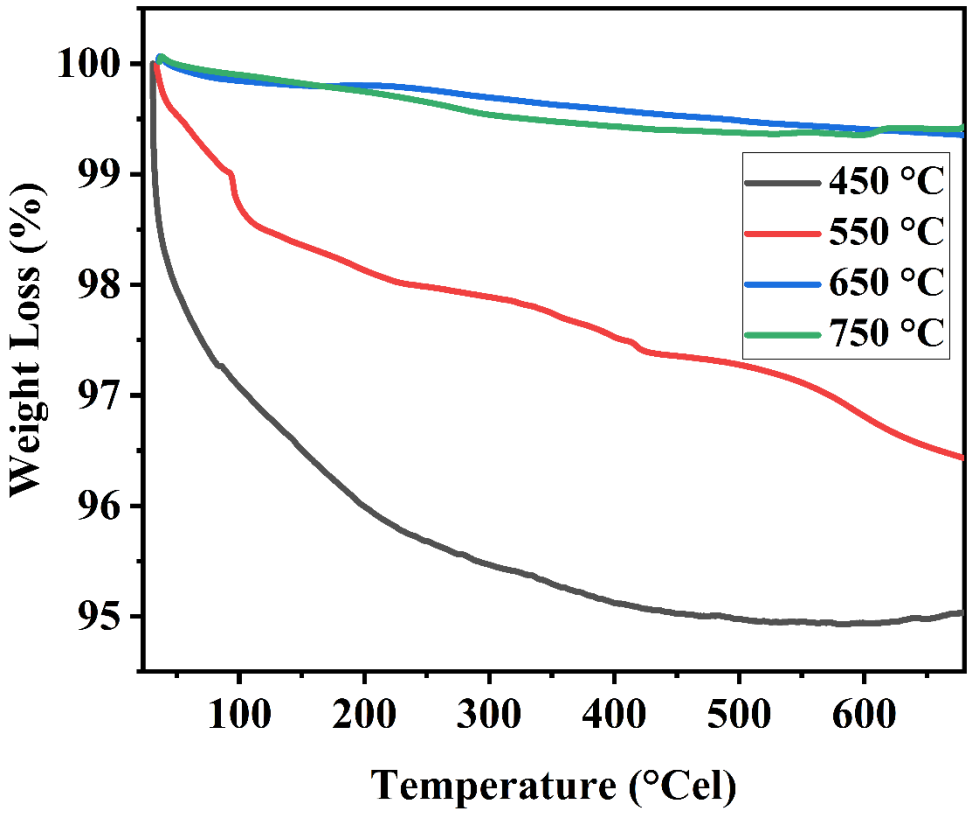

Figure 7. TGA curves of TiO_2 nanoparticles annealed at 450, 550, 650, and 750 °C

For the sample annealed at 650 °C, the TGA curve shows a minimal weight loss (~1%), indicating a highly stable structure. A minor weight reduction around ~171 °C corresponds to the removal of residual surface-bound species, while a slight fluctuation near ~571 °C may be attributed to lattice relaxation or phase transformation-related rearrangements. Beyond these minor variations, the curve remains nearly stable, confirming that most volatile and organic components have already been eliminated. The final weight retention of approximately 99.35% demonstrates significant thermal robustness and structural densification at this temperature[4,28].

At 750 °C, the TGA curve exhibits negligible overall weight loss (~0.5%), with minor fluctuations observed at ~38, 126, 264, and 437 °C. These small variations are associated with the removal of trace residual species or minor surface rearrangements. Above ~532 °C, slight irregular increase and decrease in weight are observed, which are typically attributed to instrumental baseline variations or buoyancy effects, rather than actual mass gain. The final weight remains nearly constant (~99.47%), confirming the

formation of a thermally stable, highly crystalline TiO_2 structure, consistent with complete phase transformation and densification [28].

The progressive reduction in weight loss with increasing annealing temperature confirms the removal of surface-bound species and the formation of a thermally stable TiO_2 lattice. Table 6 explains the thermal behaviour of TiO_2 nanoparticles which follows a three-stage decomposition mechanism

Table 6. Three-stage thermal decomposition mechanism of TiO_2 nanoparticles as identified from TGA curves.

Temperature Range	Process
<100 °C	Removal of physically adsorbed water
100 - 400 °C	Decomposition of organics + dehydroxylation
> 400 °C	Lattice stabilization + phase transformation

3.7. Electrochemical Properties (CV and EIS)

Cyclic voltammetry (CV) was employed to evaluate the electrochemical charge storage behaviour of the annealed samples at different temperatures (450, 550, 650, and 750 °C) over a range of scan rates (10–100 mV s^{-1}) as presented in figure 8. The calculated specific capacitance values are summarized in Table 7.

The electrochemical behaviour reflects the structural and surface modifications induced by annealing temperature. The CV curves exhibit quasi-rectangular profiles, indicating dominant capacitive behaviour with contributions from both electric double-layer capacitance (EDLC) and possible pseudocapacitive reactions, a response commonly reported for nanostructured TiO_2-based electrodes and TiO_2@C core–shell systems [14,29,30]. The absence of sharp redox peaks indicates that pseudocapacitive contributions are surface-controlled rather than diffusion-limited.

A clear dependence of specific capacitance on scan rate is observed across all samples. At 450 °C, the specific capacitance reaches a maximum value of 1.311 F g^{-1} at 10 mV s^{-1}, which progressively decreases to 0.152 F g^{-1} at 100 mV s^{-1}. This trend is consistent with electrochemical theory, where lower scan

rates allow sufficient time for electrolyte ions to diffuse into the inner active sites of the electrode, resulting in enhanced charge storage. In contrast, at higher scan rates, ion diffusion becomes kinetically limited, restricting charge storage predominantly to the outer surface and thereby reducing the measured capacitance [29,31–33].

Furthermore, a systematic decrease in capacitance is observed with increasing annealing temperature. The 450 °C sample exhibits the highest capacitance, followed by 550 °C, 650 °C, and 750 °C samples. This reduction can be attributed to thermally induced structural changes such as grain growth, reduced surface area, and possible loss of active sites at higher annealing temperatures. Increased crystallinity at elevated temperatures reduces defect density and lower electrochemically active surface area, thereby diminishing capacitance performance [6,14,34,35]

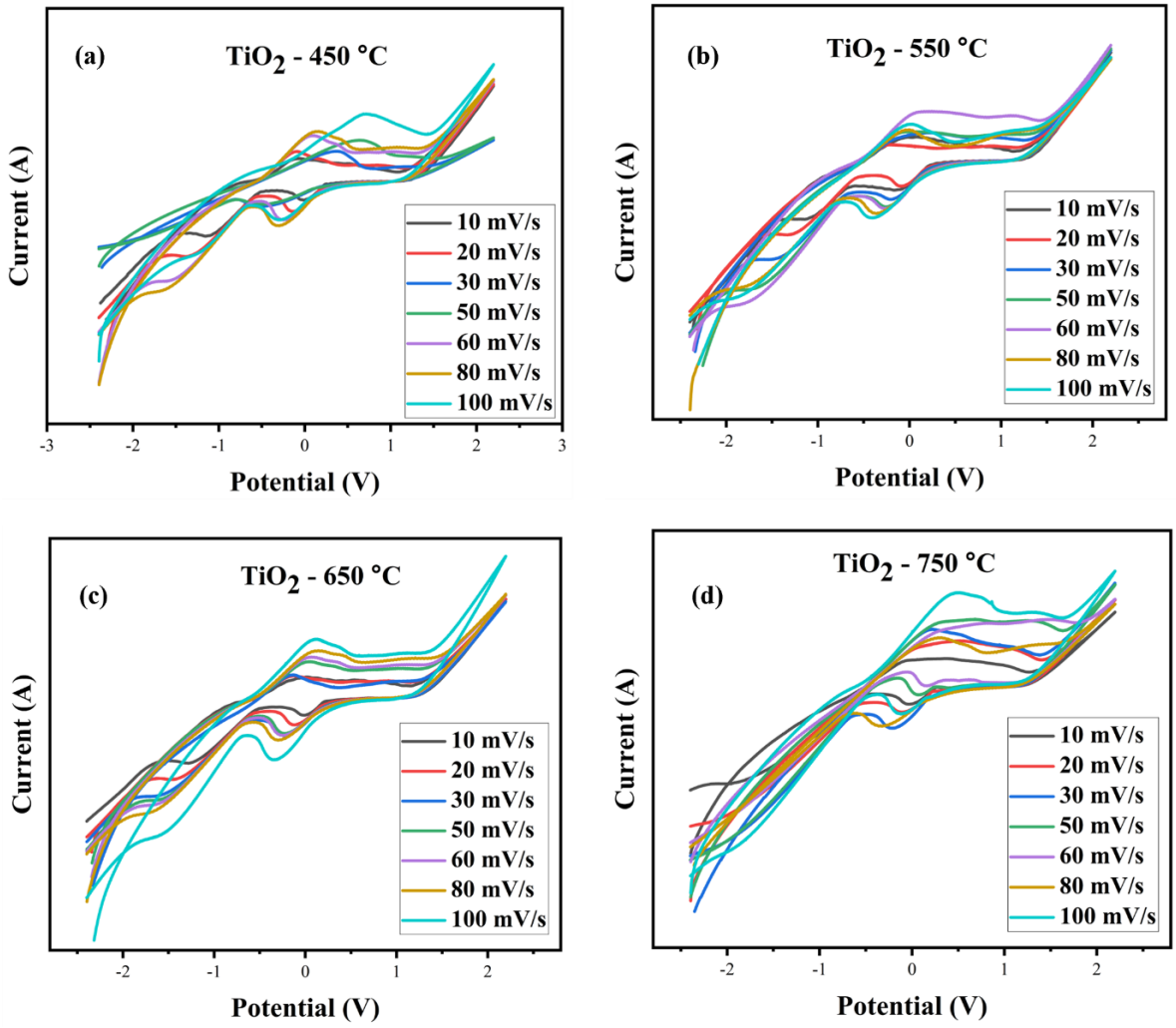

Figure 8. Cyclic voltammetry curves of TiO_2 nanoparticles annealed at 450, 550, 650, and 750 °C recorded at scan rates of 10, 20, 30, 50, 60, 80, and 100 mV s^{-1}

To further elucidate the charge transport kinetics, electrochemical impedance spectroscopy (EIS) analysis was performed and presented in Figure 9. In all cases, the Nyquist plots exhibit a depressed semicircle at high frequencies followed by a slanted line at low frequencies. This response is characteristic of an interface controlled by charge-transfer resistance (Rct) in parallel with a non-ideal double-layer capacitance, coupled to a Warburg-type diffusion element at lower frequencies, as commonly described for porous and rough electrodes [36,37]. The Nyquist plots reveal that the 450 °C sample exhibits the lowest charge transfer resistance, while the 750 °C sample shows significantly higher resistance due to structural densification and reduced active surface area. This observation strongly correlates with the CV results, where the 450 °C sample demonstrated the highest specific capacitance, confirming that improved conductivity and ion diffusion at lower annealing temperatures facilitate enhanced electrochemical performance [6,36,37].

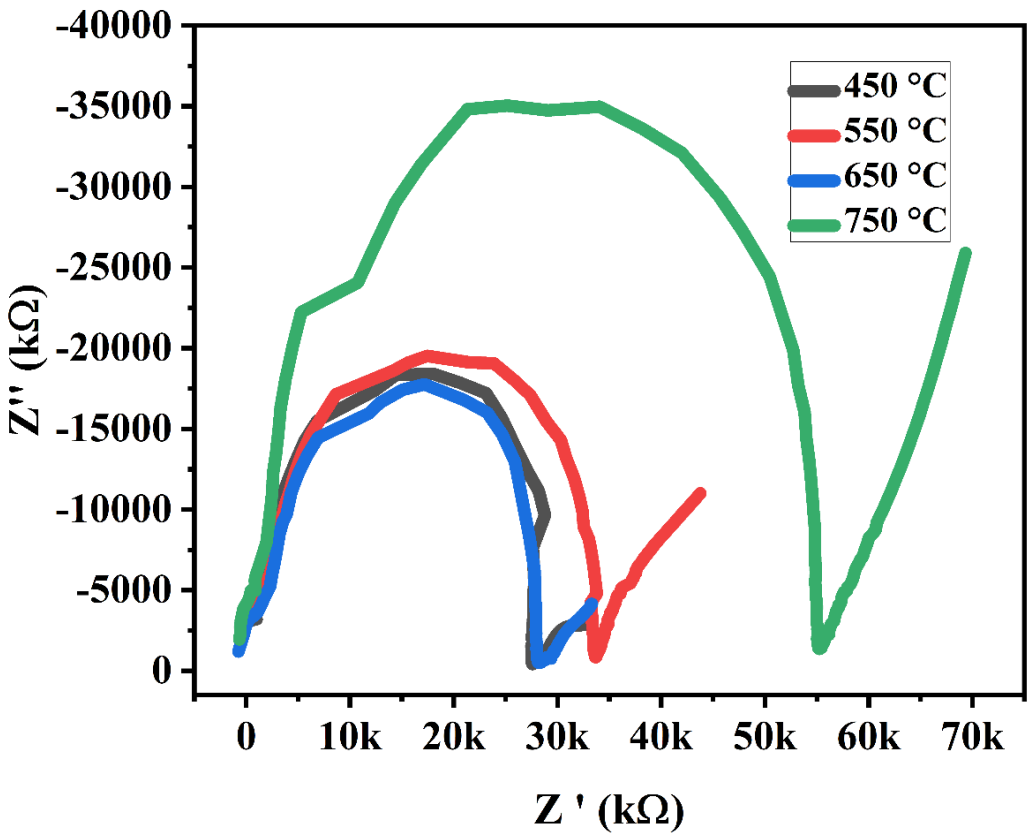

Figure 9. EIS Nyquist plots of TiO_2 nanoparticles annealed at 450, 550, 650, and 750 °C

Overall, the CV results confirm that both scan rate and annealing temperature significantly influence electrochemical performance. The superior capacitance at lower scan rates and lower annealing temperature (450 °C) indicates enhanced ion accessibility and optimal surface characteristics, making it the most electrochemically favourable condition among the studied samples [6,14,34,35].

Table 7. Specific capacitance of TiO_2 nanoparticles annealed at 450, 550, 650, and 750 °C at scan rates of 10–100 mV s^{-1}, determined from cyclic voltammetry.

Sample	Scan Rate mV s^{-1}	Specific Capacitance F g^{-1}
450 °C annealed TiO_2	10	1.311
	20	0.708
	30	0.273
	50	0.161
	60	0.252
	80	0.204
	100	0.152
550 °C annealed TiO_2	10	1.623
	20	0.642
	30	0.500
	50	0.347
	60	0.296
	80	0.224
	100	0.174
650 °C annealed TiO_2	10	1.116
	20	0.549
	30	0.401
	50	0.234

Sample	Scan Rate mV s^{-1}	Specific Capacitance F g^{-1}
650 °C annealed TiO_2	60	0.208
	80	0.169
	100	0.178
750 °C annealed TiO_2	10	0.956
	20	0.673
	30	0.523
	50	0.286
	60	0.211
	80	0.171
	100	0.147

3.8. Antibacterial activity

Based on its higher surface activity and defect-rich structure, the 450 °C-annealed TiO_2 sample was selected for antibacterial evaluation. The zones of inhibition (ZOI) are listed in Table 8 and the corresponding plates are shown in Figure 9. The antibacterial activity was evaluated against *Staphylococcus aureus (gram positive)*, *Bacillus subtilis (gram positive)*, and *Klebsiella pneumoniae (gram negative)* using the disc diffusion (Kirby–Bauer) method on Müeller–Hinton agar, with a standard antibiotic as control. ZOI of 9, 7, and 7 mm were observed, respectively, compared to 21–25 mm for the standard. All measurements were performed under dark conditions [15,38], indicating contact-mediated antibacterial activity rather than photocatalysis. The slightly higher inhibition against *S. aureus* is consistent with the greater susceptibility of Gram-positive bacteria [39].

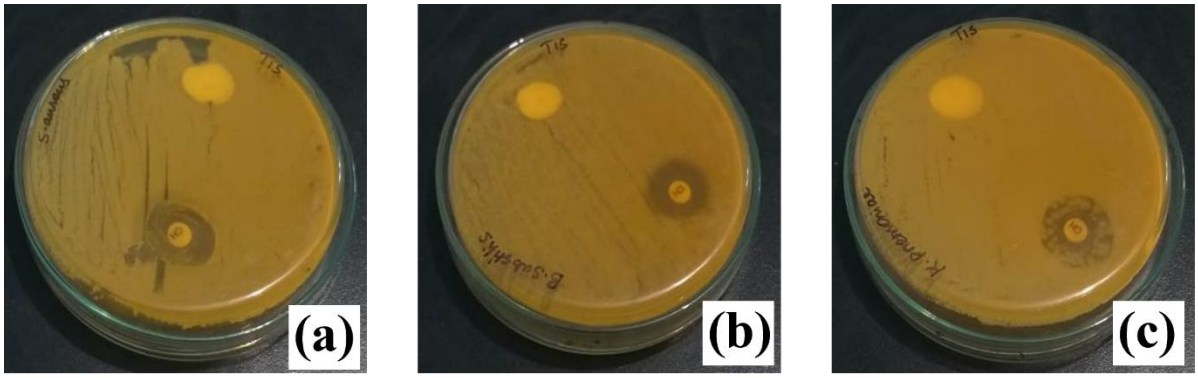

Figure 10. Disc diffusion plates showing zones of inhibition for TiO2 nanoparticles annealed at 450 °C (a) *S. aureus*, (b) *B. subtilis*, and (c) *K. pneumoniae*

The observed antibacterial behaviour correlates with the structural features of the 450 °C sample, including smaller crystallite size of 21.3 nm, higher surface hydroxyl density evident by FTIR and TGA, and lower charge-transfer resistance relevant by EIS. These factors promote reactive oxygen species (ROS) generation at the surface, leading to bacterial cell membrane disruption. is behaviour is further supported by the PL results, where defect-related emissions indicate the presence of oxygen vacancies that can facilitate enhanced ROS generation [16,40]. Notably, these same characteristics also contribute to its superior electrochemical performance, highlighting the multifunctional potential of defect-rich anatase TiO_2 for both electrochemical and antibacterial applications[40].

Table 8. Zone of inhibition (mm) recorded for TiO_2 nanoparticles annealed at 450 °C

Bacterium	TiO_2 ZOI (mm)	Standard ZOI (mm)
S. aureus	9	21
B. subtilis	7	22
K. pneumoniae	7	25

4. Conclusion

The present study systematically elucidates the temperature-driven phase evolution and associated property changes in sol–gel-derived TiO_2 nanoparticles annealed between 450 and 750 °C. XRD and Raman analyses confirm a clear structural transition from phase-pure anatase at 450–550 °C to a mixed anatase–rutile phase at 650 °C, followed by complete transformation to rutile at 750 °C. This phase evolution is accompanied by progressive crystallite growth. A strong correlation between structure and functional properties is observed across all characterization techniques. The optical absorption edge exhibits a systematic red-shift with temperature, consistent with increased crystallite size and rutile phase formation. FTIR and TGA results collectively confirm progressive dehydroxylation, removal of residual organics, and improved thermal stability at higher annealing temperatures. Photoluminescence analysis reveals a transition from visible to near-infrared emission, followed by intensity quenching at 750 °C due to reduced defect density. Although the 550 °C sample exhibits the highest specific capacitance, the 450 °C sample demonstrates superior energy storage characteristics due to its higher defect density, greater electrochemically active surface area, and lower charge-transfer resistance, which facilitate efficient ion diffusion and charge propagation. Thus, 450 °C anatase sample further demonstrates contact-mediated antibacterial activity against *S. aureus*, *B. subtilis*, and *K. pneumoniae*, with ZOI values consistent with reported data for unirradiated anatase TiO_2, confirming that its defect-rich nanostructure is advantageous across electrochemical, optical, and antibacterial applications. In contrast, higher annealing temperatures reduce capacitance due to grain growth and surface area loss. Overall, lower annealing temperatures favor electrochemical energy storage, while higher temperatures yield structurally stable rutile suitable for optical and high-temperature applications.

Acknowledgement

The authors CA and DS are extremely grateful for the financial assistance provided by the Tamilnadu State Council for Science and Technology under Science and Technology Project Scheme (TNSCST/STP/PS-01/2019-20/3676 dt. 29.03.2021).

References:

[1] D. Reyes-Coronado, G. Rodríguez-Gattorno, M.E. Espinosa-Pesqueira, C. Cab, R. De Coss, G. Oskam, Phase-pure TiO2 nanoparticles: Anatase, brookite and rutile,

Nanotechnology 19 (2008). https://doi.org/10.1088/0957-4484/19/14/145605.

[2] T. Luttrell, S. Halpegamage, J. Tao, A. Kramer, E. Sutter, M. Batzill, Why is anatase a better photocatalyst than rutile? - Model studies on epitaxial TiO2 films, Sci. Rep. 4 (2015). https://doi.org/10.1038/srep04043.

[3] D.A.H. Hanaor, C.C. Sorrell, Review of the anatase to rutile phase transformation, J. Mater. Sci. 46 (2011) 855–874. https://doi.org/10.1007/s10853-010-5113-0.

[4] H. Zhang, J.F. Banfield, Understanding Polymorphic Phase Transformation Behavior during Growth of Nanocrystalline Aggregates: Insights from TiO2, Journal of Physical Chemistry B 104 (2000) 3481–3487. https://doi.org/10.1021/JP000499J.

[5] H. Zhang, J.F. Banfield, Thermodynamic analysis of phase stability of nanocrystalline titania, J. Mater. Chem. 8 (1998) 2073–2076. https://doi.org/10.1039/a802619j.

[6] D.K. Muthee, B.F. Dejene, Effect of annealing temperature on structural, optical, and photocatalytic properties of titanium dioxide nanoparticles, Heliyon 7 (2021). https://doi.org/10.1016/j.heliyon.2021.e07269.

[7] Y. Alaya, R. Souissi, M. Toumi, M. Madani, L. El Mir, N. Bouguila, S. Alaya, Annealing effect on the physical properties of TiO2 thin films deposited by spray pyrolysis, RSC Adv. 13 (2023) 21852–21860. https://doi.org/10.1039/d3ra02387g.

[8] N. Sharma, R. Kumar, Annealing Time Effect on the Structural, Optical, and Electrical Characteristics of Titanium Dioxide Thin Films, Letters in Applied NanoBioScience 13 (2024). https://doi.org/10.33263/LIANBS134.169.

[9] N.T. Nolan, M.K. Seery, S.C. Pillai, Spectroscopic investigation of the anatase-to-rutile transformation of sol-gel-synthesized TiO2 photocatalysts, Journal of Physical Chemistry C 113 (2009) 16151–16157. https://doi.org/10.1021/jp904358g.

[10] H.C. Vasconcelos, M. Meirelles, R. Özmenteş, A. Korkut, Vacuum Ultraviolet Spectroscopic Analysis of Structural Phases in TiO2 Sol–Gel Thin Films, Coatings 15 (2025). https://doi.org/10.3390/coatings15010019.

[11] M.A. Henderson, A surface science perspective on TiO2 photocatalysis, Surf. Sci. Rep. 66 (2011) 185–297. https://doi.org/10.1016/J.SURFREP.2011.01.001.

[12] G. Busca, The surface of transitional aluminas: A critical review, Catal. Today 226 (2014) 2–13. https://doi.org/10.1016/J.CATTOD.2013.08.003.

[13] R. Plugaru, A. Cremades, J. Piqueras, The effect of annealing in different atmospheres on the lumienscence of polycrystalline TiO2, in: Journal of Physics Condensed Matter, Institute of Physics Publishing, 2004. https://doi.org/10.1088/0953-8984/16/2/031.

[14] P. Prasannalakshmi, N. Shanmugam, A.S. kumar, N. Kannadasan, Phase-

dependent electrochemistry of TiO2 nanocrystals for supercapacitor applications, Journal of Electroanalytical Chemistry 775 (2016) 356–363. https://doi.org/10.1016/J.JELECHEM.2016.06.027.

[15] A. Azam, A.S. Ahmed, M. Oves, M.S. Khan, S.S. Habib, A. Memic, Antimicrobial activity of metal oxide nanoparticles against Gram-positive and Gram-negative bacteria: a comparative study, Int. J. Nanomedicine 7 (2012) 6003–6009. https://doi.org/10.2147/IJN.S35347.

[16] B. Sohm, F. Immel, P. Bauda, C. Pagnout, Insight into the primary mode of action of TiO2 nanoparticles on Escherichia coli in the dark, Proteomics 15 (2015) 98–113. https://doi.org/10.1002/PMIC.201400101;CTYPE:STRING:JOURNAL.

[17] C. Anantha Prabhu, D. Silambarasan, R. Sarika, V. Selvam, Synthesis and characterization of TiO2, in: Mater. Today Proc., Elsevier Ltd, 2022: pp. 1793–1797. https://doi.org/10.1016/j.matpr.2022.06.074.

[18] R. Selvapriya, J. Mayandi, V. Ragavendran, V. Sasirekha, J. Vinodhini, J.M. Pearce, Dual morphology titanium dioxide for dye sensitized solar cells, Ceram. Int. 45 (2019) 7268–7277. https://doi.org/10.1016/J.CERAMINT.2019.01.008.

[19] T. Ohsaka, F. Izumi, Y. Fujiki, Raman spectrum of anatase, TiO2, Journal of Raman Spectroscopy 7 (1978) 321–324. https://doi.org/10.1002/JRS.1250070606;WGROUP:STRING:PUBLICATION.

[20] D. Bersani, P.P. Lottici, X.Z. Ding, Phonon confinement effects in the Raman scattering by TiO2 nanocrystals, Appl. Phys. Lett. 72 (1998) 73–75. https://doi.org/10.1063/1.120648.

[21] A. Di Paola, M. Bellardita, L. Palmisano, Brookite, the Least Known TiO2 Photocatalyst, Catalysts 2013, Vol. 3, Pages 36-73 3 (2013) 36–73. https://doi.org/10.3390/CATAL3010036.

[22] F. Haque, A. Blanchard, B. Laipply, X. Dong, Visible-Light-Activated TiO2-Based Photocatalysts for the Inactivation of Pathogenic Bacteria, Catalysts 14 (2024). https://doi.org/10.3390/catal14120855.

[23] P.L. Gareso, I. Mutmainnah, E. Juarlin, H. Heryanto, S. Dewang, N. Rauf, D. Tahir, P. Taba, I. Nurtanio, D. Aryanto, Enhancing photocatalytic performance of iron-doped TiO2 nanoparticles: Effects of annealing temperature on anatase-rutile mixed phase structure, Mater. Chem. Phys. 320 (2024) 129464. https://doi.org/10.1016/J.MATCHEMPHYS.2024.129464.

[24] M.S. Basir, S.N. Supardan, S.A. Kamil, M.S. Basir, S.N. Supardan, S.A. Kamil, Effect of annealing temperature on the structural, morphological, photocatalytic and optical properties of the Cu-Ni co-doped TiO2 nanoparticles, Digest Journal of Nanomaterials and Biostructures 2023 18 (3) 18 (2023) 841–857.

https://doi.org/10.15251/DJNB.2023.183.841.

[25] C. Rathore, V.K. Yadav, A. Amari, A. Meena, T. Chinedu Egbosiuba, R.K. Verma, N. Mahdhi, N. Choudhary, D.K. Sahoo, R.S. Chundawat, A. Patel, Synthesis and characterization of titanium dioxide nanoparticles from Bacillus subtilis MTCC 8322 and its application for the removal of methylene blue and orange G dyes under UV light and visible light, Front. Bioeng. Biotechnol. 11 (2023) 1323249. https://doi.org/10.3389/FBIOE.2023.1323249/FULL.

[26] H.M. Ngo, A.U. Pawar, J. Tang, Z. Zhuo, D.K. Lee, K.M. Ok, Y.S. Kang, Synthesis of Uniform Size Rutile TiO2 Microrods by Simple Molten-Salt Method and Its Photoluminescence Activity, Nanomaterials 12 (2022). https://doi.org/10.3390/nano12152626.

[27] M. Simanjuntak, I. Made Joni, F. Faizal, N. Susanto Gultom, D.-H. Kuo, C. Panatarani, J.K. Raya Bandung-Sumedang, Photoluminescence of Oxygen Vacancy-Rich Nano-TiO 2 Photocatalyst for Methylene Blue Color Degradation, n.d. https://ssrn.com/abstract=5202653.

[28] S. Bakardjieva, V. Stengl, L. Szatmary, J. Subrt, J. Lukac, N. Murafa, D. Niznansky, K. Cizek, J. Jirkovsky, N. Petrova, Transformation of brookite-type TiO2 nanocrystals to rutile: correlation between microstructure and photoactivity, J. Mater. Chem. 16 (2006) 1709–1716. https://doi.org/10.1039/B514632A.

[29] R. Sait, R. Alzahrani, N. Aslam, S. Wustoni, C. Florica, A. Diaz-Gaxiola, G. Melinte, Y. Zhang, Y. Yuan, M.N. Hedhili, S. Govindarajan, A. Syed, I. Eddine-Gallouzi, S. Inal, H. Aljawhari, Electrochemical behavior and biocompatibility of TiO2@C core–shell NWs deposited by PECVD for cellular interface application, RSC Adv. 15 (2025) 34960–34975. https://doi.org/10.1039/D5RA05460E.

[30] A. Mir, M.A. Shah, Cyclic voltammetry response of TiO2 nanostructures prepared via fast and facile microwave irradiation, Bulletin of Materials Science 2022 45:3 45 (2022) 119-. https://doi.org/10.1007/S12034-022-02703-7.

[31] M. Opitz, J. Yue, J. Wallauer, B. Smarsly, B. Roling, Mechanisms of Charge Storage in Nanoparticulate TiO2 and Li4Ti5O12 Anodes: New Insights from Scan rate-dependent Cyclic Voltammetry, Electrochim. Acta 168 (2015) 125–132. https://doi.org/10.1016/J.ELECTACTA.2015.03.186.

[32] S. Sun, Y. Sun, J. Wen, B. Zhang, X. Liao, G. Yin, Z. Huang, X. Pu, MoO3−x-deposited TiO2 nanotubes for stable and high-capacitance supercapacitor electrodes, RSC Adv. 8 (2018) 21823–21828. https://doi.org/10.1039/C8RA02744G.

[33] C. Costentin, Electrochemical Energy Storage: Questioning the Popular v/v1/2 Scan Rate Diagnosis in Cyclic Voltammetry, J. Phys. Chem. Lett. 11 (2020) 9846–9849.

https://doi.org/10.1021/ACS.JPCLETT.0C02667.

[34] H. Kang, W. Tian, J. Wu, Y. Zhang, Z. Li, G. Pang, Effect of Annealing on Microstructure and Capacitance Properties of Sol-gel TiO2 Film on Aluminum, Int. J. Electrochem. Sci. 16 (2021) 150963. https://doi.org/10.20964/2021.01.21.

[35] N. Rathore, A. Kulshreshtha, R.K. Shukla, D. Sharma, Study on morphological, structural and dielectric properties of sol-gel derived TiO2 nanocrystals annealed at different temperatures, Physica B Condens. Matter 582 (2020) 411969. https://doi.org/10.1016/J.PHYSB.2019.411969.

[36] A.C. Lazanas, M.I. Prodromidis, Electrochemical Impedance Spectroscopy─A Tutorial, ACS Measurement Science Au 3 (2023) 162–193. https://doi.org/10.1021/ACSMEASURESCIAU.2C00070.

[37] N.O. Laschuk, E.B. Easton, O. V. Zenkina, Reducing the resistance for the use of electrochemical impedance spectroscopy analysis in materials chemistry, RSC Adv. 11 (2021) 27925–27936. https://doi.org/10.1039/D1RA03785D.

[38] B. Moongraksathum, J.Y. Shang, Y.W. Chen, Photocatalytic Antibacterial Effectiveness of Cu-Doped TiO2 Thin Film Prepared via the Peroxo Sol-Gel Method, Catalysts 2018, Vol. 8, Page 352 8 (2018) 352. https://doi.org/10.3390/CATAL8090352.

[39] M.J. Hajipour, K.M. Fromm, A. Akbar Ashkarran, D. Jimenez de Aberasturi, I.R. de Larramendi, T. Rojo, V. Serpooshan, W.J. Parak, M. Mahmoudi, Antibacterial properties of nanoparticles, Trends Biotechnol. 30 (2012) 499–511. https://doi.org/10.1016/j.tibtech.2012.06.004.

[40] M. Pelaez, N.T. Nolan, S.C. Pillai, M.K. Seery, P. Falaras, A.G. Kontos, P.S.M. Dunlop, J.W.J. Hamilton, J.A. Byrne, K. O'Shea, M.H. Entezari, D.D. Dionysiou, A review on the visible light active titanium dioxide photocatalysts for environmental applications, Appl. Catal. B 125 (2012) 331–349. https://doi.org/10.1016/J.APCATB.2012.05.036.